

Black hole masses and starbursts in X-shaped radio sources

M. Mezcua¹*, A.P. Lobanov¹, V.H. Chavushyan², and J. León-Tavares^{1,2,3}

¹ Max Planck Institute for Radio Astronomy, Auf dem Hügel 69, 53121 Bonn

² Instituto Nacional de Astrofísica, Óptica y Electrónica, Apdo. Postal 51, 72000 Puebla, México

³ Aalto University Metsähovi Radio Observatory, Metsähovintie 114, FIN-02540 Kylmälä, Finland

Preprint online version: April 29, 2019

ABSTRACT

It has been suggested that the X-shaped morphology observed in some radio sources can reflect either a recent merger of two supermassive black holes (SMBHs) or the presence of a second active black hole in the galactic nucleus. These scenarios are tested by studying the relationship between the black hole mass, radio and optical luminosity, starburst history and dynamic age of radio lobes in a sample of 31 X-shaped radio galaxies drawn from a list of 100 X-shaped radio source candidates identified from the FIRST survey. The same relationships are also studied in a control sample consisting of 39 radio-loud active nuclei with similar redshifts and optical and radio luminosities. The X-shaped objects are found to have statistically higher black hole masses and older starburst activity compared to the objects from the control sample. Implications of these findings are discussed for the black hole merger scenario and for the potential presence of active secondary black holes in post-merger galaxies.

Key words. Galaxies: kinematics and dynamics – Galaxies: formation – Galaxies: nuclei – Black hole physics

1. Introduction

X-shaped (or ‘winged’) radio galaxies are a class of extragalactic radio sources with two low-surface-brightness radio lobes (the ‘wings’) oriented at an angle to the active, or high-surface-brightness, lobes. Both sets of lobes often pass symmetrically through the center of the host galaxy that is the source of the lobes, giving the galaxy an X-shaped morphology as seen on radio maps. Several authors have attempted to explain the unusual structure in X-shaped sources. The first attempt was made by Rees (1978), who suggested that the jet direction precesses due to the accretion of gas with respect to the central black hole axis. Subsequently, four different scenarios were proposed for the formation of such peculiar radio morphology: (1) backflow from the active lobes into the wings (Leahy & Williams 1984; Capetti et al. 2002); (2) slow conical precession of the jet axis (Parma, Ekers & Fanti 1985; Mack et al. 1994); (3) reorientation of the jet axis during which flow continues; and (4) reorientation of the jet axis, but the jet turned off or at greatly reduced power during the change of direction (Dennett-Thorpe et al. 2002). Merritt & Ekers (2002) suggested that the reorientation of a black hole spin axis due to a minor merger may lead to a sudden flip in the direction of any associated jet. In this case, X-shaped galaxies would be the sites of spin-flips associated with recent coales-

cences of pairs of supermassive black holes (SMBHs) (Gopal-Krishna et al. 2003; Gergely & Biermann 2009). The older wings would then represent relics of past radio jets, while the active lobes would reflect the activity following the black hole merger. Hence, synchrotron ageing should lead to a steeper spectral index in the wings or low-surface brightness features than in the high-surface brightness active lobes. However, in some X-shaped sources the wings have similar or even flatter spectral index than the active lobes (Lal & Rao 2005). To explain this discrepancy Lal & Rao (2005) suggested that at least some of the X-shaped sources may contain coalescing binary AGN systems with two pairs of jets associated with two unresolved AGNs. The activity of the secondary black holes in post-merger galaxies is suggested to depend on the linear separation and mass ratio of the two SMBH (Lobanov 2008), with equal mass mergers providing the longest time during which both SMBH remain active.

In all of these schemes the properties of the nuclear region will be affected by the past SMBH merger or the presence of a secondary SMBH. All schemes described above imply that X-shaped objects are the product of major mergers, which should then be reflected statistically in the masses of the central black holes. If X-shaped morphology is indeed caused by a profound event in the nuclear region, such as a merger of two SMBH, then it may also be reflected in the starburst history of the host galaxy. Investigations of these properties can address the question of the physical nature of the X-shaped sources and their

* mmezcu@mpifr.de Member of the International Max Planck Research School (IMPRS) for Astronomy and Astrophysics at the Universities of Bonn and Cologne.

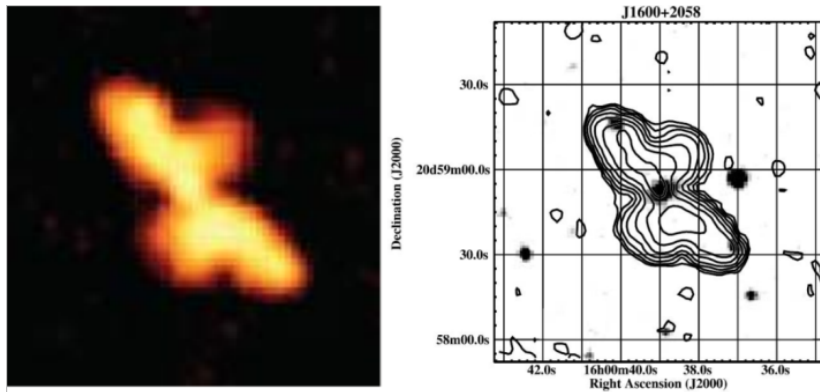


Fig. 1: Radio and optical images of one of the 100 X-shaped radio source candidates (J1600+2058). Left, color image from the VLA FIRST survey at 1.4 GHz. Right, FIRST contours overlaid on the optical image (adapted from Cheung 2007).

difference from the “canonical” radio galaxies, if representative samples of both radio types are studied and compared against each other.

In this paper we determine the black hole mass, luminosity, starburst activity and jet dynamic age of the active galaxy nuclei (AGN) of a sample of X-shaped galaxies and compare the results with those obtained for a control sample of radio-loud active nuclei with similar redshifts and optical and radio luminosities.

We employ two different methods to obtain kinematic estimates of the central black hole masses. The first method is based on the empirical correlation between BH masses and stellar velocity dispersion (Gebhardt et al. 2000; Ferrarese & Merritt 2001; Tremaine et al. 2002) as represented by stellar absorption lines in optical spectra. The second method uses motions of ionized gas near the SMBH (Peterson & Wandel 1999; Kaspi et al. 2000; Onken et al. 2004; Peterson et al. 2004) and the relation between the width of broad emission lines emitted by this gas, the BH mass, and the size of broad line regions (BLRs) estimated from the continuum luminosity (Kaspi et al. 2000, 2005).

Both methods are based on the assumption of virialized motions in the nuclear regions of galaxies, but the broad line emission reflects gas motions only around presently active black holes, while the stellar absorption lines can probe both active and inactive black holes. Therefore, the determination and comparison of the masses obtained using these two methods, the luminosities, the starburst activity, and the jet dynamic age can provide a useful tool for distinguishing between different scenarios proposed for the X-shaped objects.

The target and control samples used for the study are introduced in Section 2. Section 3 describes the data analysis and determination of the black hole masses and dynamic ages of the radio emission for both samples. Results of these measurements are presented in Section 4. A discussion of the results and their broader implication is given in Section 5.

Throughout this paper we assume a Λ cold dark matter (CDM) cosmology with parameters $H_0 = 73 \text{ km s}^{-1} \text{ Mpc}^{-1}$, $\Omega_\Lambda = 0.73$ and $\Omega_m = 0.27$.

2. The sample

The sample of AGN analysed in this paper is drawn from a list of known X-shaped sources and a list of 100 ‘winged’ and X-shaped radio source candidates (Cheung 2007) morphologically identified from the VLA FIRST survey (Becker et al. 1995).

Of the 100 X-shaped candidates, 22 were spectroscopically identified in the Sloan Digital Sky Survey (SDSS) data release (DR6; Adelman-McCarthy et al. 2008) and 27 were spectroscopically observed by Cheung et al. (2009) with the 9.2 m Hobby-Eberly Telescope (HET) at McDonald Observatory and the 6.5 m Multiple-Mirror Telescope (MMT) at Mt. Hopkins Observatory. From these lists, we have selected objects with well-detected stellar absorption lines. Our final sample comprises 20 X-shaped radio sources with SDSS spectra complemented by five of the 27 X-shaped objects with spectra presented in Cheung et al. (2009), and six of the previously known X-shaped radio sources: 3C192, 4C+32.25, 4C+48.29 and 1059+169 (Lal & Rao 2007), 3C223.1 (Lal & Rao 2005) and 4C+01.30 (Wang et al. 2003) with spectra also available in the SDSS.

In order to evaluate results obtained for the X-shaped radio galaxies, we selected a control sample of 19 radio-loud sources from Marchesini et al. (2004) plus 6 Fanaroff-Riley type II (FR II) sources from de Vries et al. (2006), and 14 radio loud elliptical galaxies from González-Serrano & Carballo (2000) that have similar redshifts ($z < 0.3$) and luminosities and whose spectra are found in the SDSS.

The X-shaped and control sample share a common range of optical and radio luminosities that covers $\log \lambda L_{5100\text{\AA}} \in [43.0, 46.0]$ and $\log \nu L_{1.4\text{GHz}} \in [39.0, 44.5]$. According to the statistical Kolmogorov-Smirnov test (KS-test) the two samples are insignificantly different in this common range.

3. Data Analysis

The optical spectra of the objects in both samples have been used to measure properties of broad H β (or H α , whenever the

H β line is too weak) emission lines and a number of stellar absorption lines. These measurements are applied to making kinematic mass estimates of the central black holes. The fits to absorption lines have also been used to recover starburst histories in the host galaxies and estimate the epochs of the most recent starburst. Angular sizes of active lobes and inactive wings (in X-shaped objects) have been measured in order to determine dynamic ages of the radio emission in the X-shaped objects and in the objects from the control sample.

3.1. Stellar absorption lines

The SDSS spectra collected for the objects in both samples contain several significant stellar absorption features (such as Ca H+K $\lambda\lambda$ 3969, 3934, the Mg I b $\lambda\lambda$ 5167, 5173, 5184 triplet, and the Ca II $\lambda\lambda$ 8498, 8542, 8662 triplet, etc.) that can be matched against a combination of different synthetic stellar template spectra, yielding an estimate of the stellar velocity dispersion.

For this task we use the stellar population synthesis code STARLIGHT (Asari et al. 2007; Cid Fernandes et al. 2004, 2005, 2007; Mateus et al. 2006). STARLIGHT uses the stellar library from Bruzual & Charlot (2003) and models the observed spectrum, O_λ , by a linear combination of simple stellar populations (SSPs). The resulting model spectrum, M_λ , is:

$$M_\lambda(x, M_{\lambda_0}, A_V, v_*, \sigma_*) = M_{\lambda_0} \left[\sum_{j=1}^{N_s} x_j b_{j,\lambda} r_\lambda \right] \otimes G(v_*, \sigma_*), \quad (1)$$

where $b_{j,\lambda} \equiv L_{\lambda}^{SSP}(t_j, Z_j) / L_{\lambda_0}^{SSP}(t_j, Z_j)$ is the j th template normalized at λ_0 , x is the population vector, M_{λ_0} is the synthetic flux at the normalization wavelength, r_λ is the reddening term, A_V is the V-band extinction, and $G(v_*, \sigma_*)$ is the line-of-sight stellar velocity distribution, modeled as a Gaussian feature centered at velocity v_* and broadened by σ_* . The best fit is reached by minimizing χ^2 ,

$$\chi^2(x, M_{\lambda_0}, A_V, v_*, \sigma_*) = \sum_{\lambda=1}^{N_\lambda} [(O_\lambda - M_\lambda) w_\lambda]^2, \quad (2)$$

where the weighted spectrum w_λ is defined as the inverse of the noise in the observed spectra.

In order to assess the fidelity of the STARLIGHT fit we introduce a quality factor Q combining the reduced χ^2 parameter of the modeled spectra, the velocity dispersion, σ_* and its error, δ_* : $Q = (\chi^2 \delta_* / \sigma_*)^{-1/2}$. Fits with $Q > 10$ can be considered reliable (these are the fits with reduced χ^2 close to unity and fractional errors of the velocity dispersion of $\leq 3\%$).

For some objects with a strong continuum STARLIGHT can fail to synthesize the spectrum of the host galaxy, since the flux of the lines of the host galaxy is much fainter than the AGN continuum flux. In this case, we apply the correlation $\sigma_* = \text{FWHM}[\text{OIII}]/2.35$ obtained by Nelson (2000) assuming that $\sigma_* = \sigma_{gas}$

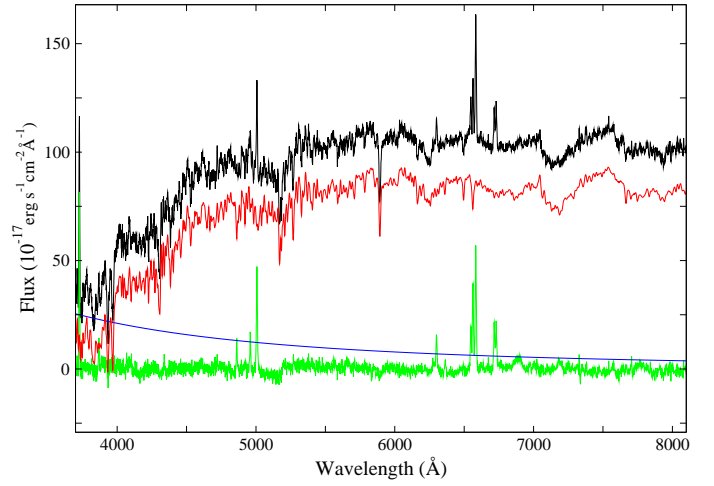


Fig. 2: STARLIGHT fit for the spectrum of the X-shaped source J1424+2637. Shown are: the observed spectrum (top black line), the modeled spectrum (second red line, displaced from observed spectrum), and the AGN continuum (blue line). The residual spectrum obtained after the subtraction of the stellar light and the continuum is shown in green (bottom line).

. The FWHM of the [OIII] line is determined from a fit to the narrow lines of the [OIII] $\lambda\lambda$ 4959, 5007Å doublet in the residual spectrum.

3.2. Emission lines

We determine properties of the broad emission lines using the residual spectra obtained after subtracting the host galaxy contribution and AGN continuum from the STARLIGHT fits. The H β and [OIII] emission lines in these spectra are modeled as a combination of narrow and broad components. We first fit three narrow Gaussian components for the oxygen [OIII]4959Å and [OIII]5007Å lines and for H β . Three additional constraints are applied during the fitting in order to reduce the number of free parameters and provide robust fits: 1) the central wavelengths of the narrow line components are set to their respective laboratory wavelengths; 2) the FWHM of the two [OIII] narrow components are required to have the same value; 3) the 1:3 ratio of amplitudes of the [OIII]4959Å and [OIII]5007Å narrow components is fixed.

After adjusting the narrow components, broad Gaussian components are added to the H β line, and the joint fit is further adjusted until the relative residuals are reduced below 0.02-0.03.

Whenever the observed H β line is too weak or absent, the same fitting method is applied to the H α and [NII]6548, 6583Å emission lines. We first fit a narrow Gaussian component to each line, setting the central wavelength of each component to its respective laboratory wavelength, and then constrain the FWHM of the two [NII] components to have the same value and a ratio [NII]6548Å/[NII]6583Å of 1:3.

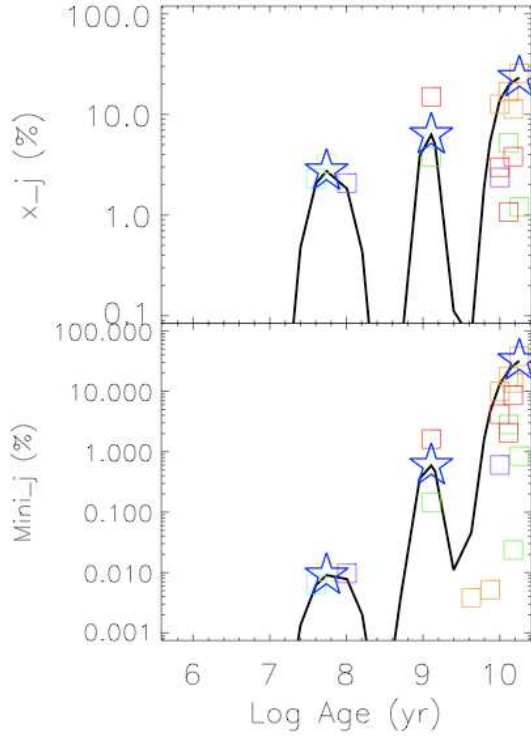


Fig. 3: STARLIGHT fits for J1327–0203: the light fraction (x_i) vs. age (top) and mass fraction $Mini_j$ vs. age (bottom) for each stellar population used. The squares correspond to stellar populations with different metallicities (in the color version: blue $0.005 Z_\odot$, purple $0.020 Z_\odot$, green $0.200 Z_\odot$, yellow $0.400 Z_\odot$, orange $1.000 Z_\odot$ and red $2.500 Z_\odot$). The solid curve represents Gaussian smoothing applied to the mass and light fraction distributions of individual starbursts. The stars indicate the resulting starburst episodes identified.

3.3. Starburst histories

The STARLIGHT model for the observed spectra also yields the light fraction x_j , mass fraction $Mini_j$, age τ_j , and metallicity Z_j , of the stellar populations used in the fit. We use these parameters to derive starburst histories and estimate the epochs of the most recent starbursts in the galaxies studied. We apply Gaussian smoothing to the individual starburst events (see Fig. 3) and determine the epoch of the most recent starburst episode.

3.4. Optical continuum

Most of the X-shaped radio sources and some objects from the control sample are obscured AGN. STARLIGHT often cannot provide reliable estimates of the AGN continuum flux for such objects. The rest-frame flux at 5100\AA is estimated for such cases from the SDSS photometry, using the following relation (Wu & Liu 2004):

$$f_{5100\text{\AA}}[\text{Jy}] = 3631 \times 10^{-0.4g} \left[\frac{4700}{5100(1+z)} \right]^{-(g-r)/2.5 \log(6231/4770)} \quad (3)$$

where z is the redshift and g and r fiber magnitudes are obtained from the SDSS and corrected for Galactic extinction A_V (taken

from Schlegel et al. 1998). It should be noted that the flux obtained using this method contains also a contribution from the host galaxy, but this does not introduce a strong bias in our estimates.

3.5. Black hole masses

The measured stellar velocity dispersion, σ_* , can be connected to the mass, M_{BH} , of the central black hole through an empirical relation (Gebhardt et al. 2000; Tremaine et al. 2002):

$$M_{\text{BH}} = 1.349 \times 10^8 M_\odot \left(\frac{\sigma_*}{200 \text{ km s}^{-1}} \right)^{4.02 \pm 0.32} \quad (4)$$

This relation is valid under the assumption that the kinematics of the stars in the bulge of the host galaxy are dominated by the gravitational potential of the central SMBH (Ferrarese & Merritt 2001).

If the FWHM of the broad emission lines reflects a Keplerian motion of ionized gas in the BLR, the mass of the central black hole can be estimated from $M_{\text{BH}} = G^{-1} R_{\text{BLR}} V_{\text{BLR}}^2$, where G is the gravitational constant, R_{BLR} is the radius of the BLR and V_{BLR} is the velocity of the line-emitting gas, traditionally estimated from the FWHM of the $H\beta$ emission line (or $H\alpha$ in the absence of $H\beta$). Kaspi et al. (2000) found that the R_{BLR} is correlated with the monochromatic continuum luminosity λL_λ at 5100\AA of the host galaxy, and Greene & Ho (2005) found a correlation between this continuum luminosity and the luminosity of the $H\alpha$ ($L_{H\alpha}$) and $H\beta$ ($L_{H\beta}$) emission lines. The black hole mass can then be expressed in terms of the observed $L_{H\beta}$ (or $L_{H\alpha}$) and the FWHM of the broad $H\beta$ (or $H\alpha$) lines, respectively (Greene & Ho 2005):

$$M_{\text{BH}} = 3.6 \pm 0.2 \times 10^6 \left(\frac{\lambda L_{H\beta}}{10^{42} \text{ erg/s}} \right)^{0.56 \pm 0.02} \left(\frac{\text{FWHM}_{H\beta}}{10^3 \text{ km/s}} \right)^2 M_\odot \quad (5)$$

$$M_{\text{BH}} = 2.0^{+0.4}_{-0.3} \times 10^6 \left(\frac{\lambda L_{H\alpha}}{10^{42} \text{ erg/s}} \right)^{0.55 \pm 0.02} \left(\frac{\text{FWHM}_{H\alpha}}{10^3 \text{ km/s}} \right)^{2.06 \pm 0.06} M_\odot \quad (6)$$

3.6. Dynamic age of radio lobes

The dynamic age t_a of the high-surface-brightness (active) radio lobes is obtained from their angular size θ_a , defined as the separation between the center of the radio source and the most distant contour in the FIRST image. The dynamic age is then given by θ_a/v_a , where v_a is the lobe advance speed (we adopt the commonly assumed $v_a \approx 0.1 c$; cf., Tingay et al. 1998). Assuming that the fuelling of the low-surface-brightness lobes of the X-shaped sources had stopped after the high-surface ones were activated, the dynamic age of the passive lobes t_p during their active stage can be estimated as

$$t_p = \frac{\theta_p - t_a v_p}{v_a}, \quad (7)$$

where θ_p is the angular size of the low-surface brightness lobes and v_p is their expansion speed during the inactive stage. In the absence of an observational estimate for v_p , we use $v_p = 0.01 c$ in our calculation. It should be noted that reducing v_p further has

only a small effect on the ages derived for the passive lobes. The total dynamic age of the X-shaped sources can then be obtained from the sum of the dynamic ages of the active and passive lobes.

4. Results

Combined results from fitting the optical spectra, black hole mass calculations, and age measurements for the radio lobes and most recent starbursts are presented in Tables 1–3.

Tables 1 and 2 list (for the X-shaped objects and the control sample, respectively) stellar velocity dispersions (col. 2), black hole masses derived from σ_* (col. 3), optical luminosities of the AGN (col. 4) and of the host galaxies (col. 5), radio luminosities (col. 6), dynamic ages of the radio lobes (col. 7), most recent starburst ages (col. 8), spectroscopic redshifts (col. 9), and quality factors of the STARLIGHT fit (col. 10). For the X-shaped sources, the total (active + passive lobe) age of the radio emission is given in brackets in col. 7.

The X-shaped sources J1625+2705 and J1015+5944 and the control sample objects 1217+023, 2247+140, 2349-014, 1004+130, 3C277.1 and 3C254 are quasars with strong power-law continuum in their spectra. For these objects, STARLIGHT cannot provide robust fits for stellar absorption lines. Estimates of σ_* are obtained in these cases using the correlation $\sigma_* = \text{FWHM}[\text{OIII}]/2.35$ (Nelson 2000). The STARLIGHT results for two further X-shaped sources (J0941-0143 and J1348+4411) have provided unreliable σ_* fits and are excluded from further analysis.

Table 3 lists the FWHM of the $H\beta$ broad line component (Col. 2) and the black hole mass calculated using Eq. 5 and Eq. 6 (Col. 3). Since there are too few objects with emission lines, only in four X-shaped sources could the FWHM of the $H\beta$ broad line be measured. In the case of the control sample, fourteen FWHMs were measured. The BH mass obtained from the FWHM (M_{BH} FWHM) reflects the presence of an active black hole, while the mass derived from the stellar velocity dispersion (M_{BH} starlight) probes both active and inactive black holes. The four X-shaped sources with broad emission lines seem to have higher M_{BH} (starlight) than M_{BH} (FWHM), while this is not observed for all the fourteen control sources. The low number of sources that show broad emission lines does not allow us to statistically compare these BH masses. This study will be pursued when more X-shaped spectra are available.

5. Discussion

Based on the results summarized in the previous section, we can now study the black hole mass distribution, the starburst activity and the evolution of radio emission in X-shaped radio galaxies as compared to galaxies hosting the “canonical” radio sources.

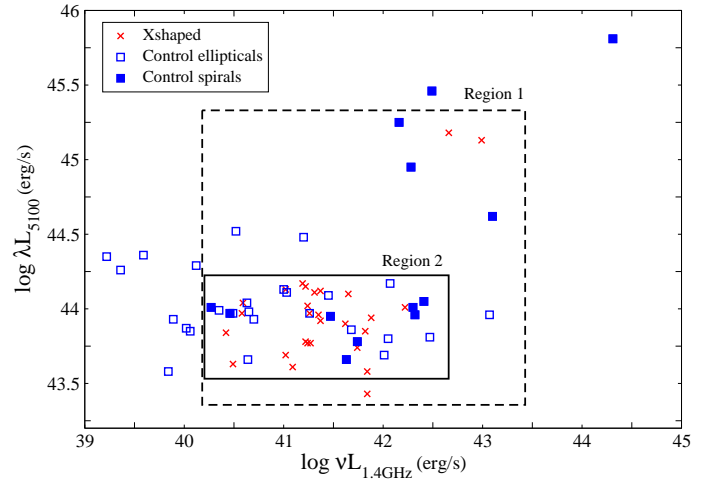


Fig. 4: Optical continuum luminosity versus radio luminosity at 1.4 GHz for X-shaped sources (crosses), control ellipticals (filled squares), and control spirals (empty squares). Dashed square: first common range of optical and radio luminosities, called Region 1. Black rectangle: tighter range of luminosities, called Region 2. The Region 2 is further divided into two bins providing the tightest luminosity match between the target and control samples.

5.1. Luminosity matching

To assess the matching between the X-shaped radio galaxies sample with the control sample, we plot the continuum luminosity derived from the SDSS magnitudes (Eq. 3) versus the radio luminosity at 1.4 GHz in Fig. 4. In order to reduce the potential influence of outlier objects on the results, we consider three different regions in the luminosity space.

The entire original radio-optical luminosity range, including all the sources, is designated hereafter Region 0. To provide a tighter match between the samples (at the expense of reducing the sample sizes), we define two smaller subregions or windows (shown in Fig. 4). Region 1 ranges from $\log \lambda L_{5100\text{\AA}} \in [43.0, 45.3]$ to $\log \nu L_{1.4\text{GHz}} \in [40.25, 43.25]$ and excludes mainly the control sources with the lowest radio luminosities since there are no X-shaped sources with such low luminosities. Region 2 covers the ranges of $\log \lambda L_{5100\text{\AA}} \in [43.5, 44.25]$ and $\log \nu L_{1.4\text{GHz}} \in [40.25, 42.5]$. In both Regions 1 & 2 the X-shaped and control samples are similar, with a statistical difference not higher than 1.2σ .

Table 1: X-shaped objects

Name (1)	σ_* (km/s) (2)	$\log\left(\frac{M_{BH} \text{ starlight}}{M_\odot}\right)$ (3)	$\log\left(\frac{\lambda L_{5100\text{\AA}} \text{ AGN}}{\text{erg/s}}\right)$ (4)	$\log\left(\frac{\lambda L_{5100\text{\AA}} \text{ galaxy}}{\text{erg/s}}\right)$ (5)	$\log\left(\frac{\nu L_{1.4 \text{ GHz}}}{\text{erg/s}}\right)$ (6)	$\log\left(\frac{\text{dynamic age}}{\text{yrs}}\right)$ (7)	$\log\left(\frac{\text{starburst age}}{\text{yrs}}\right)$ (8)	redshift (9)	Q (10)
1059+169	220.98 ± 6.42	8.30 ± 0.05	41.01 ± 5.18	43.69	41.02	6.62 (6.98) ^f	6.00	0.069	60.03
3C192	209.94 ± 7.97	8.21 ± 0.07	- ^b	43.85	41.82	6.52 (6.71) ^f	6.70	0.060	41.46
3C223.1	196.90 ± 9.14	8.10 ± 0.08	42.30 ± 0.87	43.94	41.88	6.44 (6.78) ^f	9.11	0.107	35.30
4C+01.30	151.86 ± 6.78	7.65 ± 0.08	43.12 ± 0.15	44.10	41.65	6.24 (6.61) ^f	9.40	0.132	24.88
4C+32.25	194.80 ± 6.21	8.08 ± 0.06	42.42 ± 0.14	43.97	41.26	6.69 (6.85) ^f	6.50	0.051	59.44
4C+48.29	194.30 ± 7.94	8.08 ± 0.07	42.28 ± 0.19	43.78	41.22	6.72 (7.02) ^f	8.46	0.053	38.82
J0001-0033	277.32 ± 4.55	8.70 ± 0.03	- ^b	43.77	41.27	6.37 (6.60) ^f	6.50	0.247	83.94
J0049+0059	282.23 ± 9.64	8.73 ± 0.06	- ^b	43.43	41.84	6.68 (6.83) ^f	9.20	0.304	31.07
J0813+4347	251.25 ± 5.79	8.53 ± 0.04	- ^b	44.11	41.31	6.29 (6.49) ^f	9.10	0.128	44.69
J0838+3253	241.60 ± 11.43	8.46 ± 0.08	- ^b	43.92	41.37	6.59 (6.76) ^f	8.50	0.213	28.77
J0859-0433	250.37 ± 12.90	8.52 ± 0.09	42.33 ± 2.65	- ^c	42.13	6.08 (6.65) ^f	8.00	0.356	24.55
J0924+4233	231.16 ± 15.72	8.38 ± 0.12	- ^b	43.58	41.84	6.54 (6.77) ^f	9.00	0.227	15.96
J0941-0143	154.92 ± 20.61	7.68 ± 0.23	42.48 ± 5.15	43.19	42.84	6.14 (6.64) ^f	7.00	0.384	4.92 ^e
J1005+1154	272.88 ± 6.46	8.67 ± 0.04	- ^b	44.12	41.37	6.43 (6.67) ^f	9.10	0.166	66.08
J1015+5944	285.86 ^a ± 3.90	8.75 ± 0.02	- ^b	45.18	42.66	6.67 (6.88) ^f	- ^d	0.527	- ^d
J1040+5056	211.57 ± 15.88	8.23 ± 0.13	- ^b	43.77	41.24	6.44 (6.65) ^f	9.20	0.154	20.74
J1043+3131	195.27 ± 8.24	8.09 ± 0.07	41.15 ± 1.15	43.63	40.49	5.80 (6.09) ^f	6.80	0.036	32.66
J1111+4050	254.75 ± 4.96	8.55 ± 0.03	- ^b	44.17	41.19	6.16 (6.43) ^f	6.50	0.074	74.31
J1140+1057	196.37 ± 7.80	8.10 ± 0.07	40.51 ± 20.11	43.61	41.09	6.28 (6.51) ^f	6.00	0.081	40.99
J1207+3352	181.28 ± 3.79	7.96 ± 0.04	41.85 ± 0.84	44.13	41.02	6.19 (6.44) ^f	6.00	0.079	51.36
J1210-0341	221.29 ± 9.90	8.30 ± 0.08	42.14 ± 2.94	43.90	41.62	5.97 (6.56) ^f	8.70	0.178	33.61
J1210+1121	223.51 ± 9.41	8.32 ± 0.07	- ^b	43.96	41.35	6.66 (6.78) ^f	7.60	0.196	33.55
J1327-0203	237.30 ± 9.27	8.43 ± 0.07	- ^b	44.01	42.22	6.39 (6.65) ^f	7.70	0.183	38.98
J1330-0206	219.35 ± 7.72	8.29 ± 0.06	- ^b	44.04	40.59	6.35 (6.61) ^f	7.00	0.087	42.40
J1339-0016	323.77 ± 4.55	8.97 ± 0.02	- ^b	44.15	41.22	6.55 (6.81) ^f	8.50	0.145	88.09
J1348+4411	108.42 ± 27.71	7.05 ± 0.45	41.67 ± 10.43	43.28	41.63	5.87 (6.53) ^f	6.90	0.267	2.95 ^e
J1424+2637	174.99 ± 6.53	7.90 ± 0.07	40.48 ± 6.37	43.97	40.58	6.13 (6.37) ^f	6.50	0.037	45.36
J1444+4147	226.06 ± 9.35	8.34 ± 0.07	- ^b	43.74	41.74	6.60 (6.80) ^f	8.50	0.188	35.89
J1455+3237	224.17 ± 5.52	8.33 ± 0.04	41.57 ± 1.78	43.84	40.42	6.10 (6.31) ^f	6.50	0.084	68.39
J1614+2817	344.13 ± 6.21	9.08 ± 0.03	41.32 ± 2.65	44.02	41.24	5.59 (6.22) ^f	6.00	0.108	25.85
J1625+2705	198.30 ^a ± 4.54	8.12 ± 0.04	- ^b	45.13	42.99	6.57 (6.89) ^f	- ^d	0.526	- ^d

Column designation: (1) – object name as given by Cheung (2007); (2) – stellar velocity dispersion obtained from STARLIGHT; (3) – black hole mass obtained from σ_* ; (4) – 5100 Å continuum luminosity from STARLIGHT; (5) – 5100 Å continuum luminosity from SDSS photometry; (6) – 1.4 GHz radio luminosity; (7) – dynamic age of the active lobes; (8) – age of the most recent starburst; (9) – spectroscopic redshift from SDSS; (10) – quality factor. **Notes:** *a* – velocity dispersion obtained using the correlation $\sigma_* = \text{FWHM}[\text{OIII}]/2.35$; *b* – STARLIGHT could not fit the continuum luminosity; *c* – no SDSS photometry available; *d* – no STARLIGHT fit; *e* – low fidelity of the STARLIGHT fit; *f* – in brackets, total radio dynamic age (active + passive lobes)

Table 2: Control sample

Name	σ_* (km/s)	$\log\left(\frac{M_{BH} \text{ starlight}}{M_\odot}\right)$	$\log\left(\frac{L_{5100\text{\AA}} \text{ AGN}}{\text{erg/s}}\right)$	$\log\left(\frac{L_{5100\text{\AA}} \text{ galaxy}}{\text{erg/s}}\right)$	$\log\left(\frac{\nu L_{1.4 \text{ GHz}}}{\text{erg/s}}\right)$	$\log\left(\frac{\text{dynamic age}}{\text{yrs}}\right)$	$\log\left(\frac{\text{starburst age}}{\text{yrs}}\right)$	redshift	Q
(1)	(2)	(3)	(4)	(5)	(6)	(7)	(8)	(9)	(10)
0755+37	251.55 ± 4.63	8.53 ± 0.03	41.58 ± 0.09	44.48	41.20	6.16	6.00	0.043	85.50
1004+130	167.82 ^a ± 1.05	7.77 ± 0.01	- ^b	45.46	42.49	6.89	- ^d	0.241	- ^d
1217+023	174.94 ^a ± 1.72	7.84 ± 0.02	- ^b	45.25	42.16	6.84	- ^d	0.240	- ^d
1527+30	322.89 ± 7.49	8.97 ± 0.01	- ^b	44.29	40.12	6.38	8.20	0.114	64.60
1613+27	221.13 ± 6.13	8.31 ± 0.05	41.11 ± 0.40	43.99	40.35	5.89	6.00	0.065	58.17
2349-014	201.97 ^a ± 2.12	8.72 ± 0.01	- ^b	44.95	42.28	6.06	- ^d	0.174	- ^d
3C197.1	144.35 ± 9.53	7.56 ± 0.12	42.46 ± 0.05	43.80	42.05	6.11	6.00	0.128	17.33
3C198	164.35 ± 5.76	7.79 ± 0.06	42.46 ± 0.02	43.66	41.63	6.43	6.00	0.081	51.31
3C219	188.98 ± 8.49	8.03 ± 0.08	42.52 ± 0.07	43.96	43.07	6.94	6.00	0.174	21.14
3C223	181.42 ± 8.26	7.96 ± 0.08	42.45 ± 0.06	43.81	42.47	7.06	9.40	0.137	24.50
3C227	112.51 ± 3.35	7.13 ± 0.05	43.63 ± 0.00	43.95	41.47	6.78	6.00	0.086	24.43
3C236	247.41 ± 7.26	8.50 ± 0.05	- ^b	44.17	42.07	7.74	6.50	0.101	54.96
3C254	234.20 ^a ± 3.29	8.35 ± 0.03	- ^b	45.81	44.31	1.55	- ^d	0.736	- ^d
3C270	269.46 ± 3.72	8.65 ± 0.02	- ^b	44.04	40.63	6.12	7.00	0.007	84.46
3C277.1	235.90 ^a ± 0.57	8.37 ± 0.00	- ^b	44.62	43.10	5.04	- ^d	0.320	- ^d
3C285	162.58 ± 9.46	7.77 ± 0.10	- ^b	43.86	41.68	6.6	6.00	0.079	26.37
3C287.1	246.02 ± 7.86	8.49 ± 0.06	43.24 ± 0.04	44.01	40.27	6.82	6.00	0.216	32.12
3C303	167.41 ± 9.77	7.82 ± 0.10	43.22 ± 0.01	43.96	42.32	6.28	7.20	0.141	16.86
3C332	172.37 ± 3.80	8.64 ± 0.01	40.90 ± 4.45	44.05	42.41	6.62	6.00	0.151	33.13
4C29.47	198.73 ± 0.17	8.12 ± 0.06	- ^b	44.09	41.45	6.35	8.01	0.073	53.97
4C30.19	161.97 ± 0.06	7.76 ± 0.04	- ^b	44.11	41.03	- ^c	8.01	0.091	61.46
4C32.25	196.32 ± 0.16	8.10 ± 0.06	40.28 ± 28.98	43.97	41.26	6.61	6.00	0.051	58.20
4C36.14	256.37 ± 0.35	8.56 ± 0.04	- ^b	44.26	39.36	6.60	7.00	0.112	68.51
B2 0800+24	186.04 ± 0.13	8.00 ± 0.06	- ^b	43.85	40.06	6.42	6.50	0.043	55.56
B2 0843+31	183.02 ± 0.14	7.98 ± 0.07	- ^b	43.58	39.84	6.98	7.00	0.067	43.13
B2 1003+26	240.82 ± 0.40	8.45 ± 0.06	- ^b	44.52	40.52	7.17	9.11	0.117	38.18
B2 1102+30	262.26 ± 0.35	8.60 ± 0.04	41.14 ± 6.59	44.35	39.22	6.35	6.50	0.072	74.22
B2 1204+34	179.59 ± 0.09	7.94 ± 0.05	42.16 ± 0.03	44.13	41.00	6.46	6.00	0.079	40.96
B2 1347+28	209.58 ± 0.23	8.21 ± 0.06	- ^b	43.98	40.65	6.34	8.01	0.072	46.69
B2 1422+26B	174.49 ± 0.10	7.89 ± 0.06	40.49 ± 8.18	43.97	40.49	6.15	6.00	0.037	52.44
B2 1557+26	223.51 ± 0.24	8.32 ± 0.05	41.09 ± 15.68	43.93	39.89	- ^c	6.00	0.045	54.67
B2 1609+31	199.34 ± 0.23	8.12 ± 0.08	- ^b	43.93	40.70	5.74	6.00	0.095	31.15
J094144.82+575123.6	189.32 ± 7.83	8.03 ± 0.07	- ^b	43.97	40.46	6.43	6.00	0.159	29.56
J103143.51+522535.1	204.85 ± 11.06	8.17 ± 0.09	42.34 ± 0.10	43.69	42.01	6.42	6.00	0.166	22.09
J105500.33+520200.9	162.90 ± 12.40	7.77 ± 0.13	42.61 ± 0.11	43.78	41.74	6.46	6.00	0.187	12.12
J115409.28+023815.1	169.59 ± 11.91	7.84 ± 0.12	- ^b	43.66	40.64	6.46	6.70	0.211	18.78
J134134.85+534443.7	225.84 ± 7.07	8.34 ± 0.05	- ^b	43.87	40.02	6.55	6.00	0.141	42.80
J151215.74+020316.9	194.50 ± 10.45	8.08 ± 0.09	42.79 ± 0.09	44.01	42.30	6.52	6.00	0.219	25.33
NGC4874	251.47 ± 0.32	8.53 ± 0.04	- ^b	44.36	39.59	6.30	6.00	0.024	57.54

Column designation: (1) – object name; (2) – stellar velocity dispersion obtained from STARLIGHT; (3) – black hole mass obtained from σ_* ; (4) – 5100 Å continuum luminosity from STARLIGHT; (5) – 5100 Å continuum luminosity from SDSS photometry; (6) – 1.4 GHz radio luminosity; (7) – dynamic age of the active lobes; (8) – age of the most recent starburst; (9) – spectroscopic redshift from SDSS; (10) – quality factor. **Notes:** *a* – velocity dispersion obtained using the correlation $\sigma_* = \text{FWHM} [\text{OIII}]/2.35$; *b* – STARLIGHT could not fit the continuum luminosity; *c* – not available; *d* – no STARLIGHT fit.

Table 3: Emission lines and black hole masses

Name (1)	FWHM H β (km/s) (2)	$\log\left(\frac{M_{\text{BH}} \text{FWHM}}{M_{\odot}}\right)$ (3)
X-shaped objects		
J1015+5944	5518.45 ± 61.72	7.89 ± 0.01
J1043+3131	$1716.89^a \pm 65.29$	$5.82^b \pm 0.03$
J1625+2705	5179.77 ± 185.38	7.89 ± 0.03
4C+01.30	$2670.16^a \pm 253.99$	$7.20^b \pm 0.09$
Control sample		
0755+37	$921.70^a \pm 128.51$	$5.33^b \pm 0.13$
1004+130	6234.56 ± 76.99	8.81 ± 0.01
1217+023	3817.45 ± 128.00	8.45 ± 0.03
2349-014	6114.47 ± 178.05	8.71 ± 0.03
3C197.1	4824.11 ± 2109.38	7.64 ± 0.39
3C219	2217.94 ± 119.11	6.90 ± 0.05
3C227	4646.74 ± 85.90	7.80 ± 0.02
3C254	5861.77 ± 229.82	9.15 ± 0.03
3C287.1	2001.11 ± 34.53	6.95 ± 0.02
3C332	4349.66 ± 156.76	7.76 ± 0.03
J103143.51+522535.1	1341.75 ± 74.25	6.22 ± 0.05
J115409.28+023815.1	$1504.63^a \pm 28664.31$	$6.52^b \pm 17.04$
J134134.85+534443.7	1154.92 ± 93.32	5.88 ± 0.07
J151215.74+020316.9	1257.47 ± 233.92	6.11 ± 0.16

Notes: a – FWHM of the H α line; b – Mass determined using the $L_{\text{H}\alpha}$ and $\text{FWHM}_{\text{H}\alpha}$

5.2. Color-color diagram

The g , r and u magnitudes obtained from SDSS are plotted in a color-color diagram (see Fig. 5) for the two samples. According to the distribution of galaxies in the $u-g$ vs $g-r$ color-color diagram from Strateva et al. (2001), all galaxies lying above the $u-r = 2.22$ separator line are elliptical systems. This is the case for all the X-shaped radio sources for which the SDSS magnitudes were available. J0049+0059 was removed from the plot for having a very high value of $u-g$ ($u-g = 5.0$), but it was classified as an elliptical galaxy as well. The control sources, on the other hand, are distributed above and below the $u-r = 2.22$ separator. In order to study better the relation between the galactic hosts of the X-shaped and canonical radio sources, we will also consider two independent control subsamples of spiral and elliptical galaxies, according to their galactic type as defined by the SDSS color separation described above.

5.3. Black Hole masses

We calculate the black hole masses for all the sources using the stellar velocity dispersion and Eq. 4. In Table 4 we show the mean black hole mass for each sample and subsamples (Xshaped, control ellipticals and control spirals) and for each of the regions described above (Regions 0, 1 & 2). The ratios of the mean black hole mass defined as $r_{\text{xc}} = \langle M_{\text{BH},\text{X-shaped}} \rangle / \langle M_{\text{BH},\text{control}} \rangle$ are given as well.

Comparison of the mean black hole masses derived for the entire samples (objects in Region 0) yields ratios of mean BH

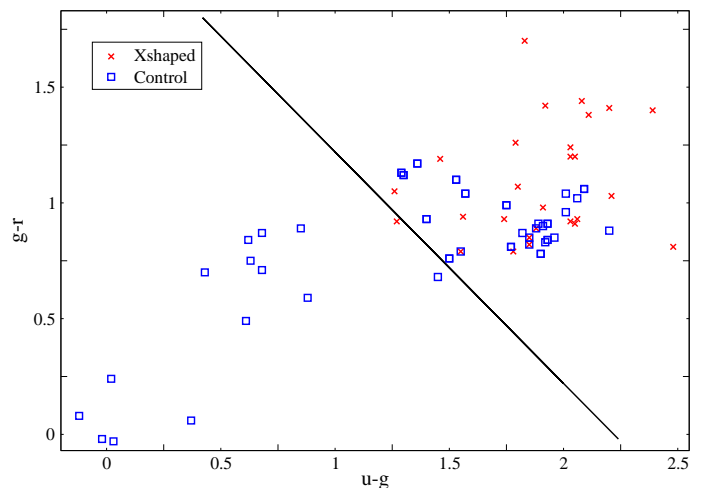


Fig. 5: Color-color diagram ($g-r$ colors versus $u-g$ colors) for X-shaped sources (cross) and control sample (square). Black line: $u-r = 2.22$ galaxy type separator from Strateva et al. (2001). Sources situated above the line are classified as elliptical while the ones under the line are spirals.

mass ranging between 1.4 for Xshaped/ellipticals to 1.9 for Xshaped/spirals.

The mass ratios derived for objects in Regions 1 and 2 are even higher, with the mean BH mass of the X-shaped sample being nearly twice the one derived for the whole control sample. In order to further reduce any potential effect of the source luminosity on the black hole mass derived, we calculate mass ratios in two smaller bins in Region 2: bin 1 ranges from $\log \nu L_{1.4\text{GHz}} \in [40.25, 41.4]$ and bin 2 from $\log \nu L_{1.4\text{GHz}} \in [41.5, 42.5]$. One can see from the resulting ratios given in Table 4 that the mass ratio does not show any evolution between the bins.

The differences in the black hole masses obtained for the X-shaped sources are further illustrated in Fig. 6 and Fig. 7 showing histograms of the mass distributions for X-shaped and control samples in Regions 0 and 2, respectively. In both regions, the X-shaped objects show a tendency of having higher black hole masses.

The KS-test applied to the BH masses of the X-shaped and control objects (ellipticals + spirals) indicates that the mass distributions are different at a statistical significance of 2.1σ . The differences are slightly larger for objects in Region 1 (2.2σ) and Region 2 (2.3σ). In Region 2 the statistical difference is as well 2.1σ when applying the KS-test to the X-shaped radio sources and the subsample of elliptical control sources.

The statistically higher black hole masses in the X-shaped objects imply that these objects are possibly located in galaxies that have undergone strong major activity in the past, with either one major merger event or multiple minor mergers.

Table 4: Mean black hole masses & mass ratios

Region		X-shaped	Control (E+S)	Control (E)	Control (S)
0	$\langle M_{\text{BH}} \rangle [M_{\odot}]$	$22.15^{+3.35}_{-2.91} \times 10^7$	$14.28^{+2.11}_{-1.84} \times 10^7$	$15.89^{+2.58}_{-2.22} \times 10^7$	$11.53^{+3.77}_{-2.84} \times 10^7$
	r_{xc}		$1.55^{+0.23}_{-0.20}$	$1.39^{+0.23}_{-0.20}$	$1.92^{+0.63}_{-0.47}$
1	$\langle M_{\text{BH}} \rangle [M_{\odot}]$	$22.15^{+3.35}_{-2.91} \times 10^7$	$12.29^{+2.07}_{-1.77} \times 10^7$	$12.79^{+2.24}_{-1.91} \times 10^7$	$11.52^{+4.42}_{-3.19} \times 10^7$
	r_{xc}		$1.80^{+0.30}_{-0.26}$	$1.73^{+0.30}_{-0.26}$	$1.92^{+0.74}_{-0.53}$
2	$\langle M_{\text{BH}} \rangle [M_{\odot}]$	$21.03^{+3.33}_{-2.87} \times 10^7$	$10.68^{+1.98}_{-1.67} \times 10^7$	$11.50^{+2.16}_{-1.82} \times 10^7$	$9.30^{+4.32}_{-2.95} \times 10^7$
	r_{xc}		$1.97^{+0.37}_{-0.31}$	$1.83^{+0.34}_{-0.29}$	$2.26^{+1.05}_{-0.72}$
2 Bin 1	$\langle M_{\text{BH}} \rangle [M_{\odot}]$	$23.39^{+4.62}_{-3.86} \times 10^7$	$13.27^{+2.80}_{-2.31} \times 10^7$	$12.43^{+2.59}_{-2.14} \times 10^7$	$7.65^{+11.63}_{-4.62} \times 10^7$
	r_{xc}		$1.76^{+0.37}_{-0.31}$	$1.88^{+0.39}_{-0.33}$	$3.06^{+4.65}_{-1.85}$
2 Bin 2	$\langle M_{\text{BH}} \rangle [M_{\odot}]$	$16.00^{+4.20}_{-3.33} \times 10^7$	$8.75^{+2.71}_{-2.07} \times 10^7$	$9.83^{+4.46}_{-3.07} \times 10^7$	$10.45^{+4.80}_{-3.29} \times 10^7$
	r_{xc}		$1.83^{+0.57}_{-0.43}$	$1.63^{+0.74}_{-0.51}$	$1.53^{+0.70}_{-0.48}$

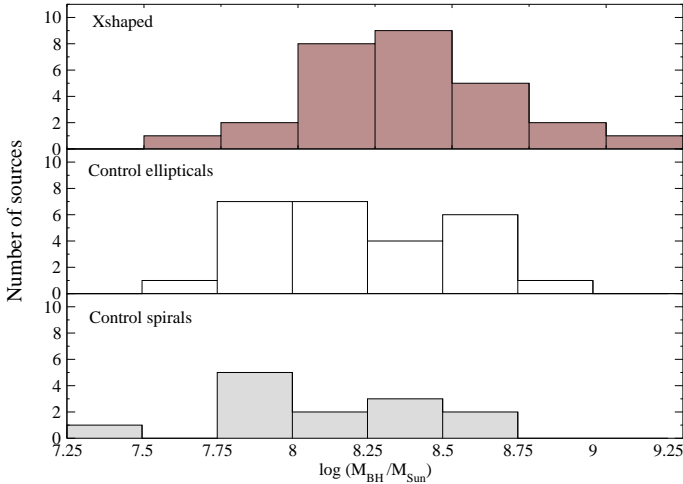


Fig. 6: Histogram of the black hole mass in Region 0 for X-shaped sources (top), control ellipticals (middle) and control spirals (bottom).

5.4. Starbursts

The starburst and radio lobe ages can be used to see whether starburst activity is different in the X-shaped objects and whether it can be related to the production of radio emission in both the target and control samples.

A histogram of the ages of the most recent starburst (Fig. 8) in the objects from Region 0 shows that a sizeable fraction of objects in both samples have relatively recent starbursts with ages of $10^{6.0}$ - $10^{6.5}$, which are possible related to the present day jet activity. However, the distribution of starburst ages in the X-shaped sample is much broader, with over half of the objects having starbursts older than 10^8 years, while only a quarter of the control

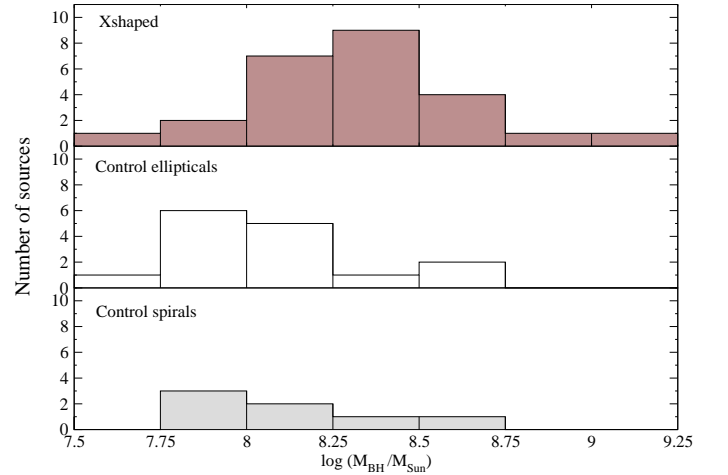


Fig. 7: Histogram of the black hole mass in Region 2 for X-shaped sources (top), control ellipticals (middle) and control spirals (bottom).

ellipticals and none of the control spirals exhibit such starbursts. Since the largest dynamic age of the active lobes is $\sim 10^7$ years (see Tables 1 and 2, col. 7), any starburst activity significantly older than 10^7 years is not likely to be related to the active lobes. It can be speculated that these older starbursts can be related to galactic mergers themselves or to the putative coalescence of the central black holes in post-merger galaxies. The latter possibility can be viably tested by comparing the starburst ages to the dynamic ages of the active and passive lobes in the X-shaped objects.

The KS-test applied to the distributions of the most recent starburst ages gives a statistical significance of 3σ for the two samples being different. To discard a possible dependence of

this difference on the galactic type, we apply the KS-test to the X-shaped sample and the subsample of control ellipticals. The results of the test show that the starburst ages of the X-shaped sources and the control ellipticals are still different at a statistical significance of 2.2σ .

In Fig. 9, histograms of the logarithm of the ratio of the dynamic age and most recent starburst age are plotted for X-shaped sources and control sources. The X-shaped sources tend to have older starburst age than dynamic age, while in both of the control subsamples these ages are comparable. The starburst activity in X-shaped sources is therefore likely not related to the active lobes. The mean logarithmic ratios are -1.29 ± 0.22 and -0.09 ± 0.16 for the X-shaped objects and the control sample, respectively. The ratio distributions are also different in the two samples at a 3σ significance. The fact that the dynamic age of the radio lobes of the control sample is similar to the most recent starburst age while X-shaped radio sources seem to have had their most recent starburst before their active lobes were formed points to a scenario in which the active lobes of the X-shaped sources are due to a possible reorientation caused by a black hole merger (Merritt & Ekers 2002) that leaves the old low-surface-brightness lobes inactive. Assuming that the low-surface-brightness lobes became inactive when the high-surface-brightness lobes were activated, the dynamic age of the passive lobes during their active stage can be determined using Eq. 7. The ratio of the total dynamic age of the active plus passive lobes and starburst age is plotted in fig. 9 (second row), obtaining that the starburst age in this reorientation scenario still remains older than the total dynamic age of the lobes. This suggests that the starburst activity in X-shaped sources had occurred before the possible reorientation due to a black hole merger, and it may have resulted from the galactic merger itself.

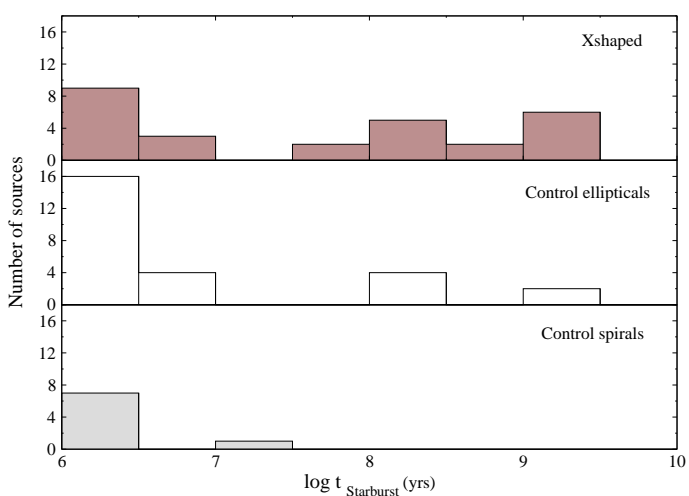


Fig. 8: Histogram of the recent starburst for X-shaped sources (top), control ellipticals (middle), and control spirals (bottom).

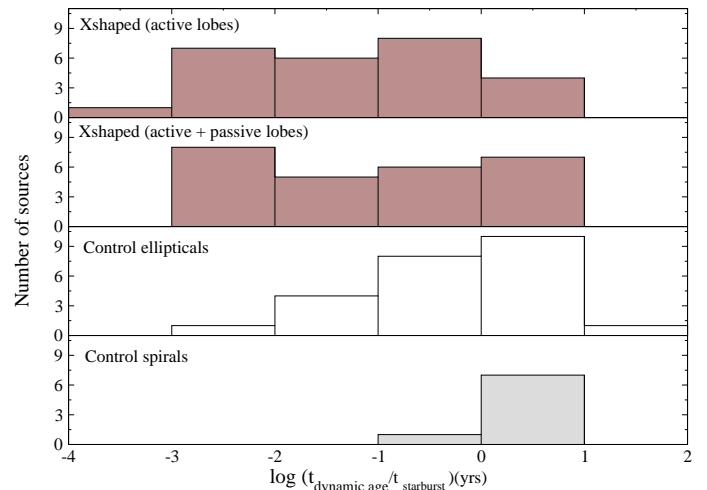


Fig. 9: Logarithmic ratios of the dynamic age of the radio emission to the age of the most recent starburst for Region 0. Top row presents the ages of active lobes in X-shaped objects, while the second row shows the sum of the ages of the active and passive lobes. The two bottom rows show distributions of the age ratios in the elliptical (third row) and spiral (fourth row) galaxies of the control sample.

6. Summary and conclusions

In this paper we have determined and studied the black hole masses and starburst histories of 31 X-shaped radio sources to look for any indications of which is the most likely scenario for the formation of their peculiar morphology. For this purpose we have compared the black hole masses and properties of the starburst activities derived for this sample to those obtained for a control sample consisting of 39 galaxies with common optical and radio luminosities. The main results of this study can be summarized as follows.

The optical colors obtained from the SDSS u, g, r photometry data indicate that all the X-shaped radio sources studied in this paper are hosted by elliptical galaxies. In the hierarchical galaxy formation model, today's galaxies are the product of frequent galaxy merging, triggering starburst and active galactic nuclei activity and possibly forming supermassive binary black hole systems (Komossa 2003). There appears to be supporting evidence that elliptical galaxies have formed from mergers in a hierarchical way (Efstathiou & Silk 1983; Toomre & Toomre 1972). Therefore the trend for X-shaped radio sources to reside in elliptical galaxies suggests that their X-shaped morphology could be related to the galaxy merger scenario.

The mean black hole mass of the objects in the X-shaped sample is statistically higher than that obtained for the control sample. This result holds for the entire range of the radio and optical luminosities as well as for smaller subranges and for exact galactic type matching between the two samples.

The statistically higher black hole masses obtained for the X-shaped objects suggest that their peculiar radio morphology can indeed result from a reorientation of the jet axis due to black hole

coalescence or from the presence of two active central engines in the nuclear region.

Comparison of starburst ages and dynamic ages of the radio lobes reveals that the most recent starburst activity in X-shaped sources is older than in the control sample and that X-shaped radio sources had their most recent starburst before their active lobes were formed. These results lend further support to the scenario in which the high-surface-brightness jets might have become active due to reorientation caused by a black hole coalescence, while the peak of starburst activity could be connected to the galactic merger itself.

7. Acknowledgments

The authors are grateful to C.C. Cheung for providing the optical spectroscopy data and to M. Karouzos for his valuable assistance. M. Mezcua was supported for this research through a stipend from the International Max Planck Research School (IMPRS) for Radio and Infrared Astronomy at the Universities of Bonn and Cologne. This work was supported by the CONACYT research grant 54480 (México). The STARLIGHT project is supported by the Brazilian agencies CNPq, CAPES and FAPESP and by the France-Brazil CAPES/Cofecub program.

References

- Adelman-McCarthy, J. K., et al. 2008, *ApJS*, 175, 297
- Antonucci, R. R. J. 1985, *ApJS*, 59, 499
- Asari, N. V., Cid Fernandes, R., Stasińska, G., Torres-Papaqui, J. P., Mateus, A., Sodré, L., Schoenell, W., Gomes, J. M. . 2007, *MNRAS*, 381, 263
- Becker, R. H., White, R. L., & Helfand, D. J. 1995, *ApJ*, 450, 559
- Bian, W., Gu, Q., Zhao, Y., Chao, L., & Cui, Q. 2006, *MNRAS*, 372, 876
- Boroson, T. A., & Green, R. F. 1992, *ApJS*, 80, 109
- Bruzual, G., & Charlot, S. 2003, *MNRAS*, 344, 1000
- Capetti, A., Zamfir, S., Rossi, P., Bodo, G., Zanni, C., & Massaglia, S. 2002, *A&A*, 394, 39
- Cheung, C. C. 2007, *AJ*, 133, 2097
- Cheung, C. C., Healey, S. E., Landt, H., Kleijn, G. V., & Jordán, A. 2009, *ApJS*, 181, 548
- Chiaberge, M., Capetti, A., & Celotti, A. 1999, *A&A*, 349, 77
- Chiaberge, M., Capetti, A., & Celotti, A. 2000, *A&A*, 355, 873
- Chiaberge, M., Capetti, A., & Celotti, A. 2002, *A&A*, 394, 791
- Cid Fernandes, R., Gu, Q., Melnick, J., Terlevich, E., Terlevich, R., Kunth, D., Rodrigues Lacerda, R., & Joguet, B. 2004, *MNRAS*, 355, 273
- Cid Fernandes, R., Mateus, A., Sodré, L., Stasińska, G., & Gomes, J. M. 2005, *MNRAS*, 358, 363
- Cid Fernandes, R., Asari, N. V., Sodré, L., Stasińska, G., Mateus, A., Torres-Papaqui, J. P., & Schoenell, W. 2007, *MNRAS*, 375, L16
- Dennett-Thorpe, J., Scheuer, P. A. G., Laing, R. A., Bridle, A. H., Pooley, G. G., & Reich, W. 2002, *MNRAS*, 330, 609
- Efstathiou, G., & Silk, J. 1983, *Fund. Cosmic Phys.*, 9, 1
- Gebhardt, K., et al. 2000, *ApJ*, 539, L13
- Gergely, L. Á., & Biermann, P. L. 2009, *ApJ*, 697, 1621
- González-Serrano, J. I., & Carballo, R. 2000, *A&AS*, 142, 353
- Gopal-Krishna, Biermann, P. L., & Wiita, P. J. 2003, *ApJ*, 594, L103
- Greene, J. E., & Ho, L. C. 2005, *ApJ*, 630, 122
- Hutchings, J. B., Frenette, D., Hanisch, R., Mo, J., Dumont, P. J., Redding, D. C., & Neff, S. G. 2002, *AJ*, 123, 2936
- Kaspi, S., Smith, P. S., Netzer, H., Maoz, D., Jannuzi, B. T., & Giveon, U. 2000, *ApJ*, 533, 631
- Kaspi, S., Maoz, D., Netzer, H., Peterson, B. M., Vestergaard, M., & Jannuzi, B. T. 2005, *ApJ*, 629, 61
- Komossa, S. 2003, *The Astrophysics of Gravitational Wave Sources*, 686, 161
- Lal, D. V., & Rao, A. P. 2005, *Astronomical Society of the Pacific Conference Series*, 345, 289
- Lal, D. V., & Rao, A. P. 2007, *MNRAS*, 374, 1085
- Leahy, J. P., & Williams, A. G. 1984, *MNRAS*, 210, 929
- Lehnert, M. D., van Breugel, W. J. M., Heckman, T. M., & Miley, G. K. 1999, *ApJS*, 124, 11
- Lobanov, A. P. 2008, *Memorie della Societa Astronomica Italiana*, 79, 1306
- Mack, K.-H., Gregorini, L., Parma, P., & Klein, U. 1994, *A&AS*, 103, 157
- McLure, R. J., & Dunlop, J. S. 2001, *MNRAS*, 327, 199
- Mateus, A., Sodre, L., Cid Fernandes, R., Stasinska, G., Schoenell, W., & Gomes, J. M. 2006, *MNRAS*, 370, 721
- Marchesini, D., Celotti, A., & Ferrarese, L. 2004, *MNRAS*, 351, 733
- Marziani, P., Sulentic, J. W., Zamanov, R., Calvani, M., Dultzin-Hacyan, D., Bachev, R., & Zwitter, T. 2003, *ApJS*, 145, 199
- Merritt, D., & Ferrarese, L. 2001, *ApJ*, 547, 140
- Merritt, D., & Ekers, R. D. 2002, *Science*, 297, 1310
- Nelson, C. H. 2000, *ApJ*, 544, L91
- Onken, C. A., Ferrarese, L., Merritt, D., Peterson, B. M., Pogge, R. W., Vestergaard, M., & Wandel, A. 2004, *The Interplay Among Black Holes, Stars and ISM in Galactic Nuclei*, 222, 109
- Parma, P., Ekers, R. D., & Fanti, R. 1985, *A&AS*, 59, 511
- Peterson, B. M., et al. 2004, *ApJ*, 613, 682
- Peterson, B. M., & Wandel, A. 1999, *ApJ*, 521, L95
- Rees, M. J. 1978, *Nature*, 275, 516
- Schlegel, D. J., Finkbeiner, D. P., & Davis, M. 1998, *ApJ*, 500, 525
- Scheuer, P. A. G. 1995, *MNRAS*, 277, 331
- Spinrad, H., Marr, J., Aguilar, L., & Djorgovski, S. 1985, *PASP*, 97, 932
- Strateva, I., et al. 2001, *AJ*, 122, 1861
- Tingay, S. J., et al. 1998, *AJ*, 115, 960
- Toomre, A., & Toomre, J. 1972, *ApJ*, 178, 623
- Tremaine, S., et al. 2002, *ApJ*, 574, 740
- de Vries, W. H., Becker, R. H., & White, R. L. 2006, *AJ*, 131, 666
- Wang, T.-G., Zhou, H.-Y., & Dong, X.-B. 2003, *AJ*, 126, 113
- Wu, X.-B., & Liu, F. K. 2004, *ApJ*, 614, 91